Magnetic phase diagram and crystal-field effects in the kagome-lattice antiferromagnet $U_3Ru_4Al_{12}$

D. I. Gorbunov,[1] I. Ishii,[2] T. Nomura,[1] M. S. Henriques,[3] A. V. Andreev,[3] M. Uhlarz,[1] T. Suzuki,[2] S. Zherlitsyn,[1] and J. Wosnitza[1,4]

[1]*Hochfeld-Magnetlabor Dresden (HLD-EMFL), Helmholtz-Zentrum Dresden-Rossendorf, 01328 Dresden, Germany*
[2]*Department of Quantum Matter, ADSM, Hiroshima University, Higashi-Hiroshima 739-8530, Japan*
[3]*Institute of Physics, Academy of Sciences, Na Slovance 2, 182 21 Prague, Czech Republic*
[4]*Institut für Festkörper- und Materialphysik, TU Dresden, 01062 Dresden, Germany*

(Received 25 November 2018; published 15 February 2019)

We report on the magnetic phase diagram of the distorted kagome-lattice antiferromagnet $U_3Ru_4Al_{12}$ determined through measurements of magnetic and elastic properties. For field applied along the [100] and [120] axes of the hexagonal crystal structure, we find pronounced anomalies in the magnetization and elastic moduli that signal the existence of unknown magnetic phases. Our crystal-electric-field (CEF) analysis evidences interlevel quadrupolar interactions between the ground-state singlet and the first excited doublet. These interactions lead to a large softening of the shear elastic modulus C_{44}. The large number of phases and pronounced elastic softening suggest that geometric frustrations and CEF effects play an important role in the physical properties of $U_3Ru_4Al_{12}$.

DOI: 10.1103/PhysRevB.99.054413

I. INTRODUCTION

Geometric magnetic frustration refers to the inability of a system to minimize the interaction energy between each pair of spins due to their spatial arrangement [1]. This lowers or even completely suppresses the magnetic ordering temperature and may reveal competing interactions and complex ground states. In a geometrically frustrated material, several spin configurations can have the same energy. A small perturbation can, therefore, significantly affect the ground state. An applied magnetic field can act as a tuning parameter between different magnetic phases. Frustrated compounds often exhibit complex phase diagrams and offer a rich playground for studying competing interactions [2–7].

Kagome systems have a corner-sharing triangular lattice. Among metallic compounds having a kagome lattice, YbAgGe stands out due to a competition of antiferromagnetic order, geometric frustration, and Kondo interactions [8–11]. Application of modest magnetic fields to YbAgGe tunes the quantum critical behavior and reveals a complex magnetic phase diagram.

Interesting physics can also be expected for metallic uranium-based kagome compounds. The $5f$ electron states are usually partially delocalized and participate in bonding. They hybridize with the s, p, and d states of surrounding atoms. The $5f$ bandwidth, the screened interatomic Coulomb interaction, the spin-orbit coupling, and the exchange interaction are all on a similar energy scale. Hence, uranium-based intermetallic compounds show a rich variety of ground states and magnetic properties (see, for instance, Ref. [12]).

The ternary intermetallic compound $U_3Ru_4Al_{12}$ crystallizes in a hexagonal crystal structure of $Gd_3Ru_4Al_{12}$ type (space group $P6_3/mmc$; a detailed description of the crystal structure is given in Refs. [13–15]) where the U atoms form a distorted kagome lattice parallel to the basal plane. This crystal structure is well suited for studying correlated magnetism in the presence of geometric frustration, as can be inferred from previous studies of isostructural compounds, particularly those with magnetic rare-earth atoms, R. Complex magnetic structures and field-induced magnetic phase transitions accompanied by large anomalies in transport and elastic properties have been reported for several members of the $R_3Ru_4Al_{12}$ family [16–23]. Although geometric frustration is likely to play a role in the magnetism of $U_3Ru_4Al_{12}$, the compound orders antiferromagnetically below 10 K [24,25]. The frustration, however, affects the magnetic structure that was found to be noncollinear with the U moments confined to the basal plane.

Here, we use magnetic field as a tuning parameter to explore the phase diagram of $U_3Ru_4Al_{12}$. We employ magnetization and ultrasound measurements in static and pulsed magnetic fields to unveil new phases in the compound. Particularly ultrasound is known to be a highly sensitive probe of magnetoelastic interactions [26–32]. We find pronounced anomalies in the magnetic and elastic properties of $U_3Ru_4Al_{12}$ that allow us to identify three ordered phases in the H-T plane for field applied along the [100] axis and two phases for field applied along the [120] direction. Additionally, our crystal-electric-field (CEF) analysis confirms that quadrupolar interactions are responsible for a pronounced softening of a shear elastic modulus. The large number of phases and the existence of quadrupolar interactions suggest that geometric frustrations and CEF effects play an important role in the physical properties of $U_3Ru_4Al_{12}$.

II. EXPERIMENTAL DETAILS

A $U_3Ru_4Al_{12}$ single crystal was grown from an 8-g quasistoichiometric mixture of the pure elements (99.9% U, 99.99% Ru, and 99.999% Al) with an Al mass excess of

1% in a tri-arc furnace by a modified Czochralski method on a rotating water-cooled Cu crucible under a protective Ar atmosphere. A tungsten rod was used as a seed. The pulling speed was 10 mm/h. Backscattered Laue diffraction was used to check the single-crystalline state and to orient the crystal for magnetic-susceptibility, magnetization, specific-heat, and ultrasound measurements.

Single-crystal x-ray diffraction data were collected at ambient temperature using a four-circle diffractometer (Gemini of Agilent) equipped with a Mo x-ray tube [$\lambda(\mathrm{MoK}\alpha) = 0.71073$ Å], a Mo-enhanced collimator, a graphite monochromator, and an Atlas CCD detector. The CRYSALIS PRO [33] program was used for lattice indexing, to refine the unit cell, to reduce the data, and to perform the absorption correction (face-indexing and Gaussian spherical harmonics algorithms). SUPERFLIP [34] was employed to solve the structure. Refinements of the crystal structure were carried out using JANA2006 [35] against all observed reflections. The final R factor for the crystal structure solved in the space group $P6_3/mmc$ (type $Gd_3Ru_4Al_{12}$) converged to 3.2%. The lattice parameters of $U_3Ru_4Al_{12}$ were found to be $a = 8.828(3)$ Å and $c = 9.430(4)$ Å, which are in good agreement with those reported in Refs. [24,25].

Magnetic susceptibility (an excitation amplitude of $\mu_0 H_{\mathrm{exc}} = 0.001$ T was applied along the [100] and [120] axes at a frequency of 97 Hz) and magnetization in static magnetic fields up to 14 T were measured using a commercial physical property measurement system (PPMS). The PPMS was also used for specific-heat measurements by the relaxation method.

High-field magnetization was measured at 2 K in pulsed magnetic fields up to 58 T by the induction method using a coaxial pickup coil system (a detailed description of the magnetometer can be found in Ref. [36]). Absolute values of the magnetization were calibrated using data obtained in static fields.

The field and temperature dependencies of the relative sound-velocity changes, $\Delta v/v$, were measured using an ultrasound pulse-echo technique [37,38] in static magnetic fields up to 17 T and in pulsed magnetic fields up to 58 T. A pair of piezoelectric transducers were glued to opposite surfaces of the sample in order to excite and detect acoustic waves. We approximated the relative changes of the elastic moduli, $\Delta C_{ii}/C_{ii}$, using $\Delta C_{ii}/C_{ii} \approx 2\Delta v_{ii}/v_{ii}$ for small sound-velocity changes. We measured the longitudinal, C_{11} ($\boldsymbol{k}$ || $\boldsymbol{u}$ || [100], where $\boldsymbol{k}$ and $\boldsymbol{u}$ are the wave vector and the polarization of acoustic waves, respectively), and C_{33} ($\boldsymbol{k}$ || $\boldsymbol{u}$ || [001]), and transverse, C_{44} ($\boldsymbol{k}$ || [100], $\boldsymbol{u}$ || [001]) and C_{66} ($\boldsymbol{k}$ || [100], $\boldsymbol{u}$ || [120]), acoustic modes. The magnetic field was applied along the [100] and [120] axes.

III. RESULTS

Figure 1(a) shows the magnetic susceptibility, χ, of $U_3Ru_4Al_{12}$ in zero field. Antiferromagnetic order sets in at around 8 K where χ starts to decrease for both the [100] and [120] excitation directions. The χ vs T data agree well with previous results and can be explained by ordering of the magnetic moments in the basal plane as found by neutron scattering [25]. [001] is the hard axis. χ does not display anomalies for H_{exc} || [001] (not shown).

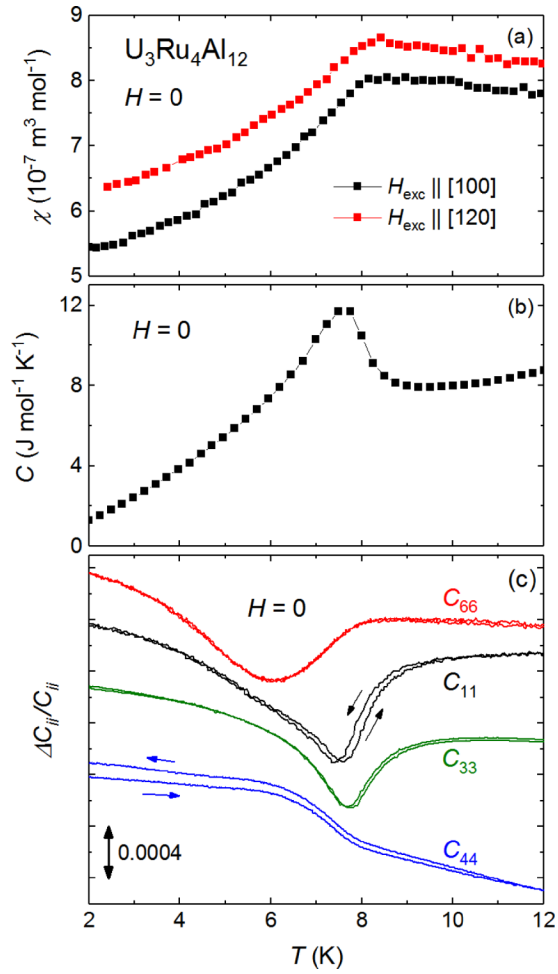

FIG. 1. Temperature dependencies of (a) the magnetic susceptibility χ, (b) the specific heat C, and (c) the relative change of the elastic moduli C_{11}, C_{33}, C_{44}, and C_{66} of $U_3Ru_4Al_{12}$ at zero field. The ultrasound frequencies were 56, 98, 29, and 124 MHz for the C_{11}, C_{33}, C_{44}, and C_{66} modes, respectively.

The specific heat, C, displays a rounded λ-type anomaly [Fig. 1(b)]. This anomaly is narrower than that reported in Ref. [25], which probably indicates a higher quality of our sample. We define the midpoint of the specific-heat increase as the Néel temperature, $T_N = 8.2$ K.

Near T_N, all elastic moduli show anomalies that evidence magnetoelastic coupling in $U_3Ru_4Al_{12}$ [Fig. 1(c)]. C_{11} and C_{33} have minima near T_N, C_{44} displays a hardening upon entering the antiferromagnetic state, and C_{66} starts to soften at T_N and shows a minimum centered at 6 K. As is shown below, the broad anomalies in C_{44} and C_{66} originate from two successive phase transitions.

In the applied field, the magnetic susceptibility does not show any clear anomaly. We used magnetization, M, and ultrasound measurements to trace the field evolution of the various magnetic phases in $U_3Ru_4Al_{12}$.

For a field of 1 T applied along the [100] axis, M/H displays a pronounced decrease on entering the antiferromagnetic state [Fig. 2(a)]. Apart from a maximum at 8 K, a small bump can be resolved near 6 K as indicated by an arrow. This suggests the presence of two transitions, which

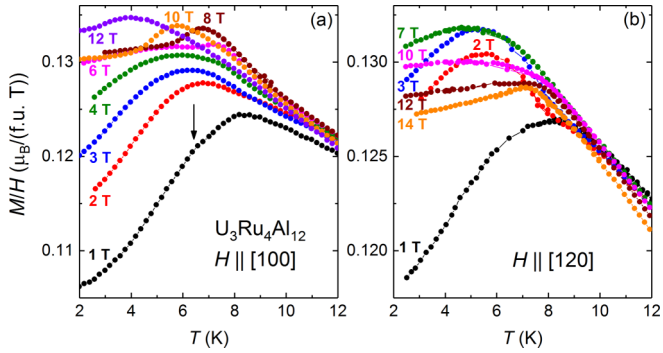

FIG. 2. Temperature dependencies of the magnetization, M, divided by the field, H, applied along the (a) [100] and (b) [120] axes of $U_3Ru_4Al_{12}$.

leads to a broad maximum in M/H in fields up to 4 T. A sharper anomaly emerges at higher magnetic fields. This anomaly appears close to T_N in zero field and, hence, signals an antiferromagnetic-paramagnetic phase transition.

M/H for field applied along the [120] axis also shows a broad maximum in 1 T [Fig. 2(b)]. The maximum shifts to lower temperatures with field up to 10 T. At higher fields, a kink is observed, e.g., at 7 K in 14 T. It likely indicates a phase transition from the antiferromagnetic into the paramagnetic state.

Thus, our magnetization data allow us to follow the field evolution of the Néel temperature and point to additional anomalies below T_N. Our measurements of elastic moduli provide further evidence for new phases in $U_3Ru_4Al_{12}$.

For field applied along the [100] axis, C_{11} and C_{33} display a minimum at the Néel temperature that broadens with increasing field [Figs. 3(a) and 3(b)]. C_{44} and C_{66} show features that provide evidence for two transitions. C_{44} shows a steplike feature in zero field and a broad maximum in applied field

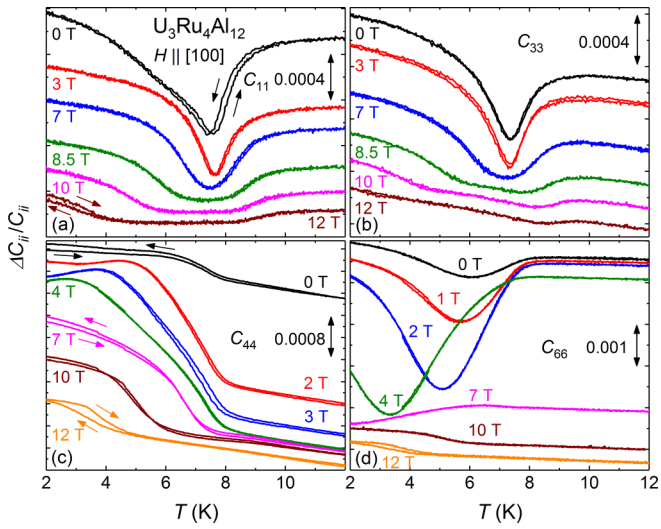

FIG. 3. Temperature dependencies of the relative change of the elastic moduli (a) C_{11}, (b) C_{33}, (c) C_{44}, and (d) C_{66} for field applied along the [100] axis of $U_3Ru_4Al_{12}$. The ultrasound frequencies were 56, 89, 29, and 124 MHz for the C_{11}, C_{33}, C_{44}, and C_{66} modes, respectively.

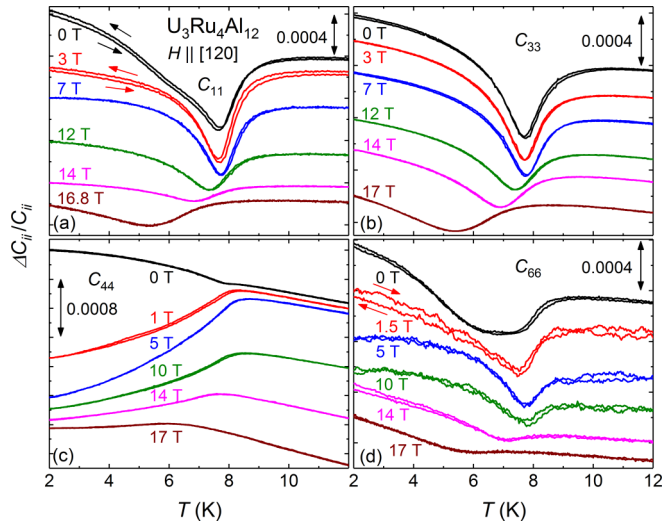

FIG. 4. Temperature dependencies of the relative change of the elastic moduli (a) C_{11}, (b) C_{33}, (c) C_{44}, and (d) C_{66} for field applied along the [120] axis of $U_3Ru_4Al_{12}$. The ultrasound frequencies were 64, 98, 30, and 112 MHz for the C_{11}, C_{33}, C_{44}, and C_{66} modes, respectively.

[Fig. 3(c)]. C_{66} shows a minimum [Figs. 3(d)]. The maximum in C_{44} and the minimum in C_{66} shift to lower temperatures with increasing field and are no longer observed above 4 T. Therefore, they most likely have an origin different from the antiferromagnetic-paramagnetic phase transition. An anomaly at T_N is seen as an inflection point in C_{44} and C_{66} up to 12 T.

All elastic moduli show a single anomaly for field applied along the [120] direction (Fig. 4). C_{11} and C_{33} exhibit a minimum near the Néel temperature that broadens and shifts to lower temperatures with increasing field [Figs. 4(a) and 4(b)]. With decreasing temperature, C_{44} shows hardening in zero field with a kink at T_N [Fig. 4(c)]. This changes to a softening below T_N and above 1 T, which suggests a large transformation of the magnetic state, probably due to a transition to a new phase. The broad minimum in C_{66} observed in zero field narrows in applied fields [Fig. 4(b)], probably due to the appearance of a new magnetic phase.

For field applied along the [100] direction at 2 K, the magnetization displays a weak change of slope near 12 T [Fig. 5(a)]. The field derivative of the magnetization, dM/dH, shows an anomaly with hysteresis at low fields and a maximum just above 12 T. Additional field-induced transitions can be revealed as well in the elastic moduli. With increasing magnetic field, C_{11} and C_{44} show hardening below 2 T at 1.4 and 1.5 K [Figs. 5(c) and 5(e)]. The hardening has large hysteresis which does not close when sweeping the field back to zero. For C_{44}, a pronounced maximum is also observed near 4 T at 1.5 K. In the same field range, C_{66} shows a broad minimum [Fig. 5(g)]. Additionally, C_{11}, C_{44}, and C_{66} display a broad hysteretic field-induced transition above 12 T as the antiferromagnetic order is suppressed [Figs. 5(c), 5(e) and 5(g)].

For field applied along the [120] axis, the magnetization is a smooth function of field up to 14 T at 2 K [Fig. 5(b)]. dM/dH shows an anomaly at 1 T. This transition leads to a

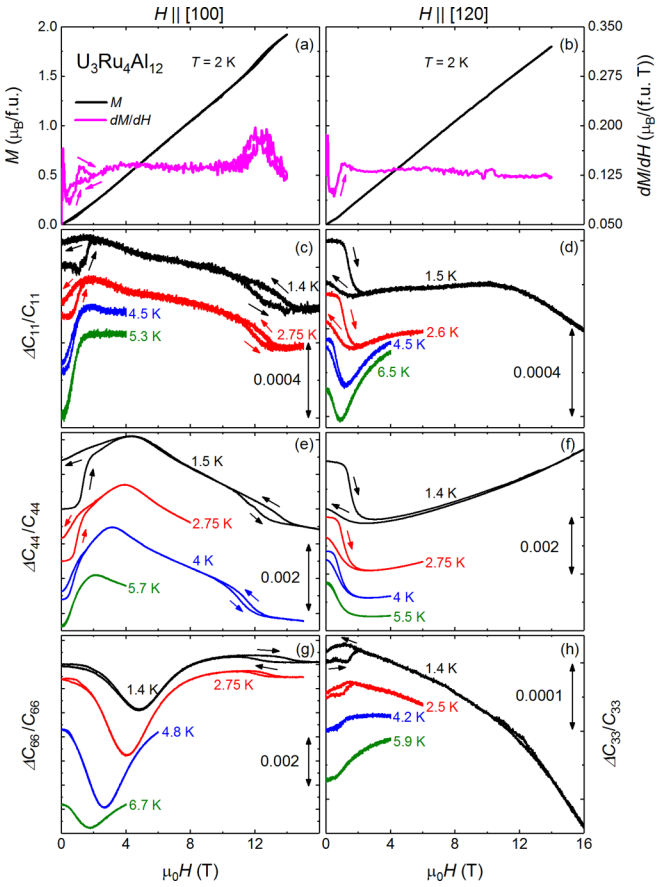

FIG. 5. Field dependencies of the magnetization, M, and the field derivative of the magnetization, dM/dH, for field applied along the (a) [100] and (b) [120] axes; and the relative change of the elastic moduli C_{11} [panels (c) and (d)], C_{44} [panels (e) and (f)], C_{66} [panel (g)], and C_{33} [panel (h)] of $U_3Ru_4Al_{12}$. For field applied along the [100] axis, the ultrasound frequencies were 56, 29, and 124 MHz for the C_{11}, C_{44}, and C_{66} modes, respectively. For field applied along the [120] axis, the ultrasound frequencies were 64, 30, and 98 MHz for the C_{11}, C_{44}, and C_{33} modes, respectively.

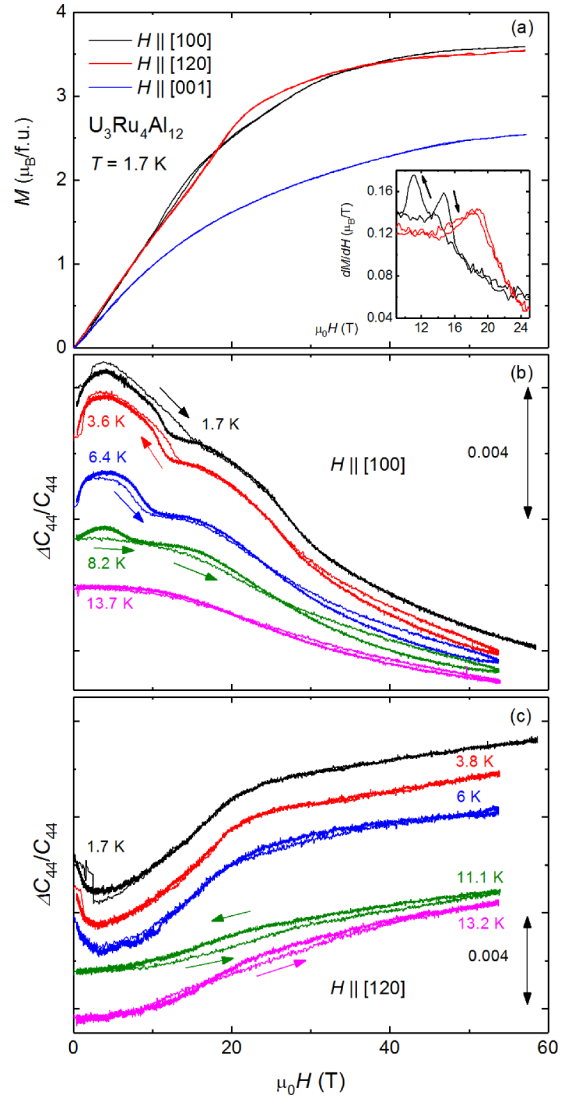

FIG. 6. Field dependencies of (a) the magnetization, M, for field applied along the [100], [120], and [001] axes and the relative change of the elastic modulus C_{44} for field applied along the (b) [100] and (c) [120] axes of $U_3Ru_4Al_{12}$. The inset in panel (a) shows the field derivatives of the magnetization, dM/dH, for field applied along the [100] and [120] axes. The ultrasound frequencies were 111 and 104 MHz for field applied along the [100] and [120] axes, respectively.

softening of C_{11} and C_{44} [Figs. 5(d) and 5(f)] and a hardening of C_{33} [Fig. 5(h)]. For C_{44}, this is in accordance with our observation that hardening changes to softening between 0 and 1 T at T_N as the temperature decreases [Fig. 4(c)]. We find no other transitions in fields up to 16 T. For C_{33} ($\boldsymbol{H}$ || [100]) and C_{66} ($\boldsymbol{H}$ || [120]), no anomalies can be resolved (not shown).

Our magnetization and ultrasound measurements in static fields up to 17 T suggest that $U_3Ru_4Al_{12}$ shows several distinct phases below T_N. We have found evidence for the existence of three magnetic phases for field applied along the [100] axis. Two phases were revealed for field applied along the [120] axis. As the magnetization does not saturate up to 17 T, higher magnetic fields are required to investigate the whole phase diagram of $U_3Ru_4Al_{12}$.

Figure 6(a) shows the magnetization measured in pulsed magnetic fields up to 58 T applied along the principal crystallographic directions of $U_3Ru_4Al_{12}$ at 1.7 K. A large magnetic anisotropy is evident between the basal plane and the [001] axis. The easy-magnetization direction lies in the basal plane, in accordance with the neutron-scattering data [25]. For $\boldsymbol{H}$ || [001], the magnetization shows no anomalies. An anomaly with hysteresis is found in the vicinity of 13 T for field applied along the [100] axis. The field derivative of the magnetization, dM/dH, shows maxima at 15 and 11 T for up and down field sweeps, respectively [inset in Fig. 6(a)]. In the same field range, C_{11}, C_{44}, and C_{66} display a broad anomaly that originates from a suppression of the antiferromagnetic order [Figs. 5(c), 5(e), and 5(g)]. For field applied along the [120] axis, dM/dH shows a maximum at 19 T. At higher fields, the magnetization for $\boldsymbol{H}$ || [100] and $\boldsymbol{H}$ || [120] shows a tendency towards saturation and reaches approximately 3.6 μ_B/f.u. Taking into account the rather large magnetic moment per uranium atom, $M_U = 2.5\ \mu_B$ [25], more transitions can be

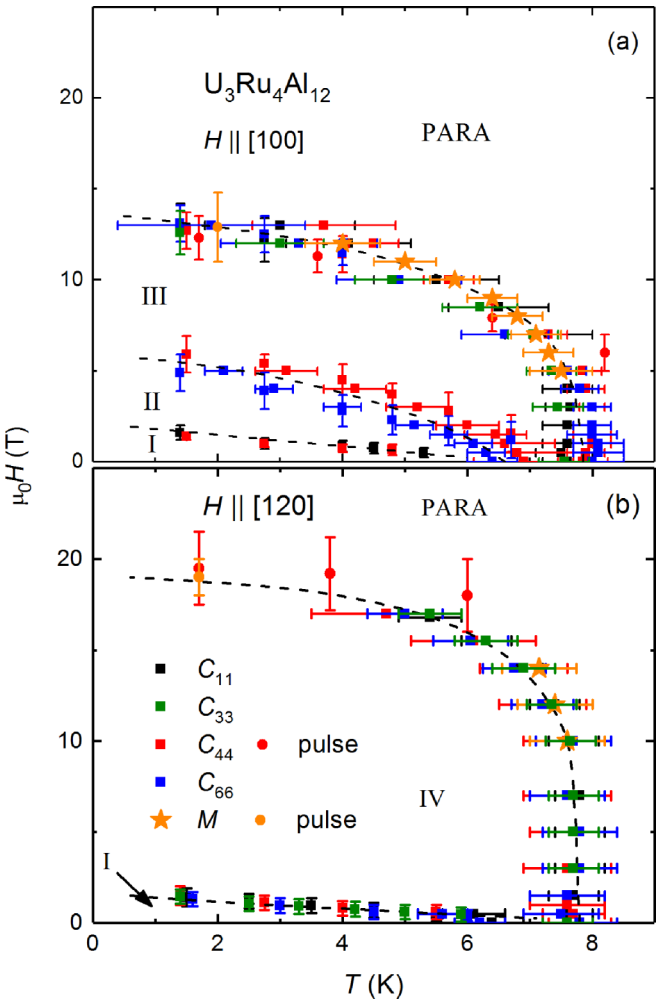

FIG. 7. Magnetic phase diagrams for field applied along the (a) [100] and (b) [120] axes of $U_3Ru_4Al_{12}$. Lines are guides to the eye.

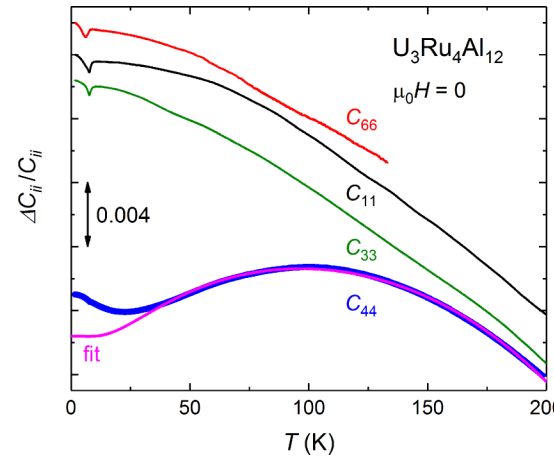

FIG. 8. Temperature dependencies of the relative change of the elastic moduli C_{11}, C_{33}, C_{44}, and C_{66} of $U_3Ru_4Al_{12}$ at zero field. The ultrasound frequencies were 64, 98, 29, and 124 MHz for the C_{11}, C_{33}, C_{44}, and C_{66} modes, respectively. The magenta curve is a fit of C_{44} using Eq. (6).

expected in higher fields, leading to a forced ferromagnetic moment of $M_{\text{ferro}} = 3 \times M_{\text{U}} = 7.5\ \mu_{\text{B}}$.

Since C_{44} displays already in static fields pronounced anomalies as a function of temperature and field, we also measured this elastic modulus in pulsed fields. C_{44} displays a softening for $\boldsymbol{H}$ || [100] in large magnetic fields [Fig. 6(b)]. In addition to the transitions found in static fields [Fig. 5(e)], we observe an inflection point between 20 and 30 T. These anomalies might indicate a crossover to a new phase. For $\boldsymbol{H}$ || [120], the softening observed in low fields is followed by a pronounced hardening [Fig. 6(c)]. A kink is seen around 20 T. Near this field, dM/dH shows a maximum [inset in Fig. 6(a)].

Figure 7 shows the H-T phase diagram of $U_3Ru_4Al_{12}$ based on our magnetization and ultrasound measurements. The diagram depends on the field direction, which points to anisotropy of the magnetic and elastic properties. For field applied along the [100] axis, three distinct phases exist below T_{N} [Fig. 7(a)]. Phase I exists in the low temperature-low field corner. With increasing field, an intermediate phase II appears at 2 T and 1.7 K. Near 6 T at low temperatures, $U_3Ru_4Al_{12}$ enters phase III. At the lowest temperatures, the antiferromagnetic-paramagnetic phase boundary is found at about 13 T.

Two phases can be found for field applied along the [120] axis [Fig. 7(b)]. Here, the ordered phase is suppressed at 19 T. Phase IV exists below the paramagnetic-antiferromagnetic phase boundary in a broad field range. Below 1.5 T, $U_3Ru_4Al_{12}$ shows phase I. A possible nature of the observed phases is discussed in Sec. V.

IV. CEF ANALYSIS

For uranium-based intermetallic compounds, CEF effects are usually not so pronounced as compared to rare-earth-based materials. This is due to the extended $5f$ wave functions in contrast to the well-localized $4f$ wave functions. Nevertheless, for some uranium-based compounds, e.g., UNiSn and UCu_2Sn, pronounced CEF effects and concomitant softening of a transverse elastic modulus have been observed [39,40].

For $U_3Ru_4Al_{12}$, there is a large softening of C_{44} below 100 K, whereas C_{11}, C_{33}, and C_{66} show hardening with decreasing temperature down to T_{N} (Fig. 8). Below, we explain this softening by CEF effects.

For a CEF analysis, we have to make an assumption about the state of the $5f$ electrons in $U_3Ru_4Al_{12}$. Previous results have shown a reduced ordered uranium magnetic moment as compared to the $5f^2$ and $5f^3$ configurations [24,25]. Additionally, the electrical resistivity is either constant or decreases strongly with temperature in the paramagnetic state, depending on the direction of current. This suggests that the $5f$ electrons are likely more delocalized at high temperatures, i.e., uranium approaches the $5f^2$ (U^{4+}) state. Therefore, we assume the $5f^2$ configuration of uranium for the CEF analysis in the paramagnetic state of $U_3Ru_4Al_{12}$.

We use the CEF model to describe our magnetization and elastic-modulus data [41,42]. We start with the effective Hamiltonian

$$H_{\text{eff}} = H_{\text{CEF}} + H_{\text{sQ}} + H_{\text{QQ}} + H_{\text{Zeeman}}, \quad (1)$$

TABLE I. CEF parameters, B_m^n (K), for $U_3Ru_4Al_{12}$.

B_2^0	B_4^0	B_6^0	B_6^6
87.9(5)	1.8(3)	−0.009(1)	0.31(3)

where $H_{\rm CEF}$, $H_{\rm sQ}$, $H_{\rm QQ}$, and $H_{\rm Zeeman}$ are the CEF, strain-quadrupole, quadrupole-quadrupole, and Zeeman energy, respectively. In the hexagonal symmetry of $U_3Ru_4Al_{12}$, the CEF term is given by

$$H_{\rm CEF} = B_2^0 O_2^0 + B_4^0 O_4^0 + B_6^0 O_6^0 + B_6^6 O_6^6, \quad (2)$$

where B_m^n are crystal-field parameters and O_m^n are Stevens' equivalent operators [43]. The strain-quadrupole interaction can be expressed as

$$H_{\rm sQ} = -\sum_i g_i O_i \varepsilon_i, \quad (3)$$

where g_i is the strain-quadrupole coupling constant, O_i is the quadrupole operator, and ε_i is the strain. The quadrupole-quadrupole interaction is

$$H_{\rm QQ} = -\sum_i g_i' \langle O_i \rangle O_i, \quad (4)$$

where g_i' is the quadrupole-quadrupole coupling constant and $\langle O_i \rangle$ is a thermal average of the operator O_i. The Zeeman energy is

$$H_{\rm Zeeman} = -g_j \mu_{\rm B} J H, \quad (5)$$

where $g_j = 0.8$ is the Landé factor and $J = 4$ is the quantum number of the total angular momentum of a U^{4+} ion.

The temperature dependence of an elastic modulus C_{ii} can be calculated using the equation

$$C_{ii}(T) = C_{ii}^{(0)}(T) - \frac{N_0 g_i^2 \chi_i^{(s)}(T)}{1 - g_i' \chi_i^{(s)}(T)}, \quad (6)$$

which takes into account quadrupolar interactions. Here, $C_{ii}^{(0)}$ is the background stiffness, $N_0 = 9.39 \times 10^{27}$ m^{-3} is the density of U atoms per unit volume, and $\chi_i^{(s)}$ is the quadrupolar susceptibility that can be extracted from the total free energy based on Eq. (1) [37]. The electron and phonon contributions to $C_{ii}^{(0)}(T)$ are given by terms proportional to T^2 and T^4, respectively [44]. Therefore, we assumed $C_{ii}^{(0)}(T)$ to be of the form

$$C_{ii}^{(0)}(T) = a + bT^2 + cT^4, \quad (7)$$

where a, b, and c are empirical coefficients. More detailed information about the CEF analysis is given in the Supplemental Material [45].

Using the CEF parameters listed in Table I, we could reproduce the measured temperature dependence of H/M between 80 and 300 K [Fig. 9(a)]. At low temperatures for field applied along the [001] axis, the calculated H/M grows, whereas the experimental H/M continues to decrease. This discrepancy can likely be explained by changes in the localization degree of the $5f$ electrons and the appearance of other contributions upon approaching the ordered state such as Kondo-like interactions [25].

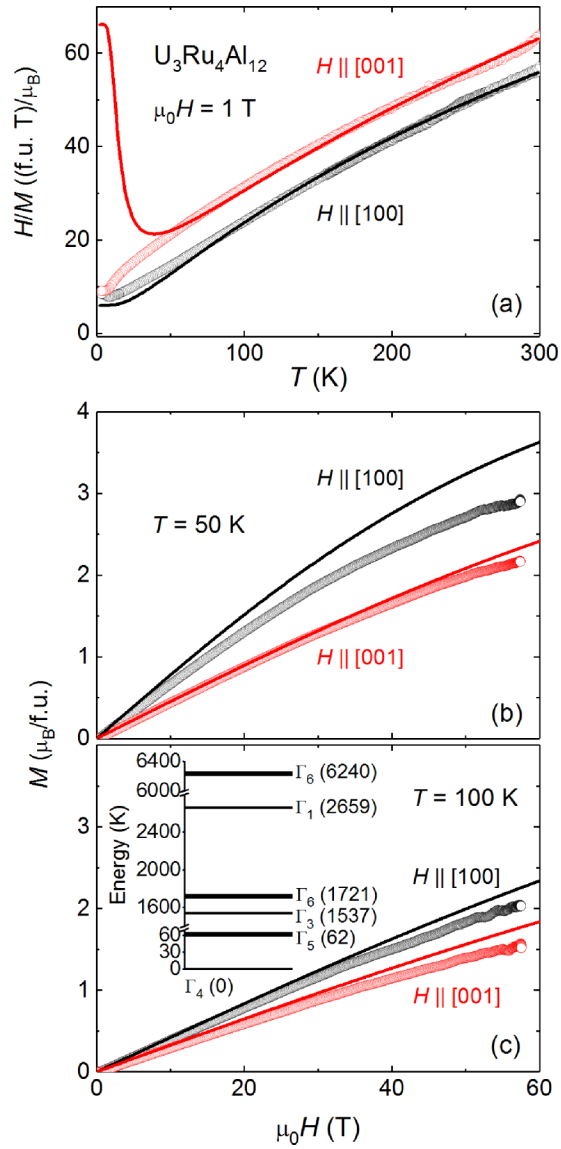

FIG. 9. (a) Temperature dependencies of H/M measured in a field of 1 T and field dependencies of the magnetization, M, up to 58 T at (b) 50 K and (c) 100 K for $U_3Ru_4Al_{12}$. In all panels, the symbols and the solid lines represent the experimental and calculated data, respectively. The inset in panel (c) shows the CEF level scheme of a U^{4+} ($J = 4$) ion obtained from the CEF parameters listed in Table I. In the inset, the thin lines represent singlets, and the thick lines represent doublets.

The magnetization in fields up to 58 T is qualitatively reproduced at 50 and 100 K [Figs. 9(b) and 9(c)]. The agreement between theory and experiment is better at 100 K.

Our model also reproduces the softening of C_{44} (Fig. 8) in the same temperature range as H/M [Fig. 9(a)]. Using Eq. (6), we obtained $g_i = 162.6$ K and $g_i' = -5.18$ K. The negative g_i' value suggests the existence of antiferroquadrupolar-type interactions.

In a hexagonal CEF, the ninefold multiplet of U^{4+} splits into three singlets and three doublets [inset in Fig. 9(c)]. The ground-state singlet Γ_4 is separated from the first excited doublet Γ_5 by 62 K. The next CEF levels have much higher

energies, beyond 1500 K. The overall CEF splitting exceeds 6000 K.

In the crystal lattice of $U_3Ru_4Al_{12}$, the matrix elements $\langle\Gamma_4|O_{yz}|\Gamma_4\rangle$ and $\langle\Gamma_4|O_{zx}|\Gamma_4\rangle$ are zero, where O_{yz} and O_{zx} are quadrupole operators. Therefore, for the ground state there is no quadrupolar degeneracy corresponding to the C_{44} mode. The energy separation between the ground state and the first excited state, 62 K, makes the existence of an interlevel quadrupolar interaction possible. The matrix elements $\langle\Gamma_4|O_{yz}|\Gamma_5\rangle$ and $\langle\Gamma_4|O_{zx}|\Gamma_5\rangle$ have nonzero values. This interlevel quadrupolar interaction explains the softening of C_{44}.

V. DISCUSSION

The electronic properties of uranium-based intermetallic compounds are largely determined by the unfilled $5f$ shell. The $5f$ wave functions are more extended as compared to the $4f$ wave functions of the rare-earth elements, resulting in a stronger hybridization with valence and conduction electrons. The $5f$ states of a vast majority of uranium intermetallics are itinerant or partly itinerant [12,46,47]. On the one hand, the extended hybridization delocalizes the $5f$ electrons and leads to a loss of magnetic order. On the other hand, it promotes magnetic coupling between the $5f$ sites. An empirical rule for the formation of the magnetic order is given by a critical value of the distance between nearest-neighbor uranium ions, known as the Hill limit [48]. If the interuranium spacing exceeds 3.4–3.6 Å, a spontaneous magnetic order of the uranium sublattice may exist. However, Hill's rule is not always valid and should rather be taken as a rule of thumb whether the $5f$ electrons can be localized (see, e.g., Refs. [49–52]).

Another important consequence of the extended hybridization of the $5f$ states is the magnetic anisotropy. It is related to the crystalline bonds in the sense that the direction of the magnetic moments is determined by the bonding symmetry. As a result, the U magnetic moments tend to align as far as possible away from the nearest-neighbor U-U links [53]. In uniaxial crystal structures, such as hexagonal and tetragonal structures, the moments are oriented perpendicular to the shortest interuranium spacings. The strong spin-orbit coupling leads to a very large magnetic anisotropy and a prevalence of collinear magnetic structures, whereby the magnetic moments are locked along high-symmetry directions.

$U_3Ru_4Al_{12}$ displays unusual magnetic properties that do not completely follow this conventional picture. The U atoms form a kagome lattice parallel to the basal plane where the shortest interuranium distances, 3.661 Å, are found. This value is above the Hill limit. $U_3Ru_4Al_{12}$ shows a rather large magnetic moment, 2.5 μ_B/U atom, as found by neutron scattering [25]. For a CEF analysis, we assumed the $5f^2$ state of uranium in the paramagnetic region and found a better agreement between experiment and theory at 100 K than at 50 K. Further, the direction of the U magnetic moments is not perpendicular to the shortest interuranium spacings. This would require the moments to be oriented parallel to the hexagonal sixfold axis. Unexpectedly, the U magnetic moments are arranged in a noncollinear triangular structure in the basal plane [25].

For $U_3Ru_4Al_{12}$, geometric frustration is lifted, which is likely due to additional interactions (exchange interactions, CEF effects, and/or spin-orbit coupling) or coupling between spins and other degrees of freedom. We can exclude a structural transition at the Néel temperature as this would undoubtedly result in much larger changes of elastic moduli. Nevertheless, the magnetoelastic coupling should not be underestimated as our ultrasound measurements provide convincing evidence for new phases in $U_3Ru_4Al_{12}$. Here, tuning of the exchange and anisotropy interactions was achieved through the application of a magnetic field. The H-T phase diagram of $U_3Ru_4Al_{12}$ features three phases for $\boldsymbol{H}$ || [100] and two phases for $\boldsymbol{H}$ || [120] below T_N.

A magnetic field applied along the hard magnetization direction of uranium intermetallic compounds with itinerant $5f$ states usually affects the directional $5f$-$5f$ bonding, e.g., the band structure [12]. The picture of localized magnetic moments forced to align along the field direction changes. The resulting M vs H dependence reflects a Pauli paramagnetic susceptibility originating from the residual density of states at the Fermi level. Therefore, it is unlikely that effects of geometric frustration will show up. The high-field magnetization of this work and the magnetoresistance of Ref. [25], both measured for field applied along the hard [001] direction of $U_3Ru_4Al_{12}$, confirm this observation.

Below, we discuss the nature of zero-field and field-induced phases in terms of their possible magnetic-moment configurations. The magnetic structure of $U_3Ru_4Al_{12}$ was determined to be commensurate noncollinear with the moments confined to the basal plane at 1.6 K [25]. The representation analysis indicates that only one two-dimensional (2D) physically irreducible representation (irrep) is active in the model described in Ref. [25] (mGM5− in the Miller and Love notation [54]). In fact, further symmetry analysis of the solution using the tools of the Bilbao Crystallographic Server [55,56] shows that the spin configuration corresponds to the Shubnikov space group $Cmcm'$, for which two different irreps are found to be active instead of one. In addition to the primary 2D irrep, mGM5−, a secondary unidimensional irrep, mGM2−, allows additional degrees of freedom for the spins in this structure. In the model described in Ref. [25], the magnetic ordering splits the magnetic site into two independent sites with distinct degrees of freedom for the U spins. Nevertheless, spin amplitude and orientation seem to be correlated with those of the primary active irrep. Hence, some relative spin orientations not forced by symmetry were probably included in the model [56], although certainly fully supported by the experimental data.

Although rare, incommensurate magnetic structures have been found for some uranium intermetallics. An incommensurate helical structure was reported for UPtGe where it forms due to the coexistence of a small in-plane magnetic anisotropy and frustrated exchange interactions [57,58]. Another example is UNiGe, which shows an incommensurate phase between 41.5 K and $T_N = 51$ K [50,59,60]. Below 41.5 K, a commensurate antiferromagnetic phase exists [50,60,61].

A small magnetic moment might be induced on the Ru atoms in applied field as well. $U_3Ru_4Al_{12}$ has a large C/T value, ≈600 mJ mol^{-1} K^{-2} [25], close to that of $Dy_3Ru_4Al_{12}$, ≈500 mJ mol^{-1} K^{-2} [16]. As explained for $Dy_3Ru_4Al_{12}$, the Ru $4d$ subsystem is involved in the exchange interactions due to a polarization originating in the $4f$ and $5d$ states. A

similar effect likely exists for $U_3Ru_4Al_{12}$, whereby the Ru $4d$ states are polarized through the $5f$ and $6d$ states. In applied field, the splitting of the spin-up and spin-down subbands of the itinerant $4d$ states grows, and the Ru magnetic moment increases.

We can speculate about an additional broad high-field feature in C_{44} in the paramagnetic state for field applied along the [100] axis [Fig. 6(b)]. It probably originates from changes of the U magnetic moment. As the magnetization continues to increase in this field range, the U moments may become more localized. If this picture is correct, the band structure should be affected. Therefore, electrical-resistivity measurements in high fields may provide more information on the physics of the $5f$ states of $U_3Ru_4Al_{12}$.

VI. CONCLUSION

Our results reveal an important role of geometric frustration and CEF effects in the physical properties of $U_3Ru_4Al_{12}$. We observed several distinct phases when the field is applied along the basal plane. Our CEF analysis suggests that the quadrupolar interactions result in a pronounced elastic softening of the shear modulus C_{44}. Thus, $U_3Ru_4Al_{12}$ is a good candidate for magnetic x-ray and neutron-scattering studies of frustration effects.

ACKNOWLEDGMENTS

The work was supported by Projects No. 16-03593S and No. 19-00925S of the Czech Science Foundation and by the Materials Growth and Measurement Laboratory (MGML, https://mgml.eu). M.S.H. acknowledges the support of the Czech Science Foundation through Project No. 19-07931Y. We acknowledge the support of HLD at HZDR, member of the European Magnetic Field Laboratory (EMFL), and the DFG through Grant No. SFB 1143.

[1] J. Wosnitza, S. A. Zvyagin, and S. Zherlitsyn, Rep. Prog. Phys. **79**, 074504 (2016).
[2] I. S. Hagemann, Q. Huang, X. P. A. Gao, A. P. Ramirez, and R. J. Cava, Phys. Rev. Lett. **86**, 894 (2001).
[3] X. G. Zheng, H. Kubozono, K. Nishiyama, W. Higemoto, T. Kawae, A. Koda, and C. N. Xu, Phys. Rev. Lett. **95**, 057201 (2005)
[4] J. S. Gardner, M. J. P. Gingras, and J. E. Greedan, Rev. Mod. Phys. **82**, 53 (2010).
[5] P. Khuntia, F. Bert, P. Mendels, B. Koteswararao, A. V. Mahajan, M. Baenitz, F. C. Chou, C. Baines, A. Amato, and Y. Furukawa, Phys. Rev. Lett. **116**, 107203 (2016).
[6] Y. Zhou, K. Kanoda, and T. K. Ng, Rev. Mod. Phys. **89**, 025003 (2017).
[7] Q. Luo, S. Hu, B. Xi, J. Zhao, and X. Wang, Phys. Rev. B **95**, 165110 (2017).
[8] S. L. Bud'ko, E. Morosan, and P. C. Canfield, Phys. Rev. B **69**, 014415 (2004).
[9] K. Umeo, K. Yamane, Y. Muro, K. Katoh, Y. Niide, A. Ochiai, T. Morie, T. Sakakibara, and T. Takabatake, J. Phys. Soc. Jpn. **73**, 537 (2004).
[10] G. M. Schmiedeshoff, E. D. Mun, A. W. Lounsbury, S. J. Tracy, E. C. Palm, S. T. Hannahs, J.-H. Park, T. P. Murphy, S. L. Bud'ko, and P. C. Canfield, Phys. Rev. B **83**, 180408(R) (2011).
[11] Y. Tokiwa, M. Garst, P. Gegenwart, S. L. Bud'ko, and P. C. Canfield, Phys. Rev. Lett. **111**, 116401 (2013).
[12] V. Sechovský and L. Havela, in *Handbook of Magnetic Materials*, edited by K. H. J. Buschow (Elsevier, Amsterdam, 1998), Vol. 11.
[13] R. E. Gladyshevskii, O. R. Strusievicz, K. Cenzual, and E. Parthé, Acta Crystallogr. Sect. B **49**, 474 (1993).
[14] J. Niermann and W. Jeitschko, Z. Anorg. Allg. Chem. **628**, 2549 (2002).
[15] N. G. Bukhan'ko, A. I. Tursina, S. V. Malyshev, A. V. Gribanov, Y. D. Seropegin, and O. I. Bodak, J. Alloys Compd. **367**, 149 (2004).
[16] D. I. Gorbunov, M. S. Henriques, A. V. Andreev, A. Gukasov, V. Petříček, N. V. Baranov, Y. Skourski, V. Eigner, M. Paukov, J. Prokleška, and A. P. Gonçalves, Phys. Rev. B **90**, 094405 (2014).
[17] S. Nakamura, S. Toyoshima, N. Kabeya, K. Katoh, T. Nojima, and A. Ochiai, Phys. Rev. B **91**, 214426 (2015).
[18] D. I. Gorbunov, M. S. Henriques, A. V. Andreev, Y. Skourski, and M. Dušek, J. Alloys Compd. **634**, 115 (2015).
[19] D. I. Gorbunov, M. S. Henriques, A. V. Andreev, V. Eigner, A. Gukasov, X. Fabrèges, Y. Skourski, V. Petříček, and J. Wosnitza, Phys. Rev. B **93**, 024407 (2016).
[20] V. Chandragiri, K. K. Iyer, and E. V. Sampathkumaran, Intermetallics **76**, 26 (2016).
[21] V. Chandragiri, K. K. Iyer, and E. V. Sampathkumaran, J. Phys.: Condens. Matter **28**, 286002 (2016).
[22] D. I. Gorbunov, T. Nomura, I. Ishii, M. S. Henriques, A. V. Andreev, M. Doerr, T. Stöter, T. Suzuki, S. Zherlitsyn, and J. Wosnitza, Phys. Rev. B **97**, 184412 (2018).
[23] I. Ishii, T. Mizuno, K. Takezawa, S. Kumano, Y. Kawamoto, T. Suzuki, D. I. Gorbunov, M. S. Henriques, and A. V. Andreev, Phys. Rev. B **97**, 235130 (2018).
[24] M. Pasturel, O. Tougait, M. Potel, T. Roisnel, K. Wochowski, H. Noël, and R. Troć, J. Phys.: Condens. Matter **21**, 125401 (2009).
[25] R. Troć, M. Pasturel, O. Tougait, A. P. Sazonov, A. Gukasov, C. Sułkowski, and H. Noël, Phys. Rev. B **85**, 064412 (2012).
[26] G. Quirion, M. L. Plumer, O. A. Petrenko, G. Balakrishnan, and C. Proust, Phys. Rev. B **80**, 064420 (2009).
[27] T. Watanabe, S. Hara, S. I. Ikeda, and K. Tomiyasu, Phys. Rev. B **84**, 020409(R) (2011).
[28] V. Tsurkan, S. Zherlitsyn, V. Felea, S. Yasin, Y. Skourski, J. Deisenhofer, H.-A. Krug von Nidda, P. Lemmens, J. Wosnitza, and A. Loidl, Phys. Rev. Lett. **106**, 247202 (2011).
[29] V. Tsurkan, S. Zherlitsyn, S. Yasin, V. Felea, Y. Skourski, J. Deisenhofer, H.-A. Krug von Nidda, J. Wosnitza, and A. Loidl, Phys. Rev. Lett. **110**, 115502 (2013).
[30] S. Zherlitsyn, V. Tsurkan, A. A. Zvyagin, S. Yasin, S. Erfanifam, R. Beyer, M. Naumann, E. Green, J. Wosnitza, and A. Loidl, Phys. Rev. B **91**, 060406(R) (2015).
[31] G. Quirion, M. Lapointe-Major, M. Poirier, J. A. Quilliam, Z. L. Dun, and H. D. Zhou, Phys. Rev. B **92**, 014414 (2015).

[32] C. Bidaud, O. Simard, G. Quirion, B. Prévost, S. Daneau, A. D. Bianchi, H. A. Dabkowska, and J. A. Quilliam, Phys. Rev. B **93**, 060404(R) (2016).
[33] CrysAlis PRO, Agilent Technologies, Version 1.171.39.46.
[34] L. Palatinus and G. Chapuis, J. Appl. Crystallogr. **40**, 786 (2007).
[35] V. Petříček, M. Dušek, and L. Palatinus, Z. Kristallogr. **229**, 345 (2014).
[36] Y. Skourski, M. D. Kuz'min, K. P. Skokov, A. V. Andreev, and J. Wosnitza, Phys. Rev. B **83**, 214420 (2011).
[37] B. Lüthi, *Physical Acoustics in the Solid State* (Springer, Heidelberg, 2005).
[38] S. Zherlitsyn, S. Yasin, J. Wosnitza, A. A. Zvyagin, A. V. Andreev, and V. Tsurkan, Low Temp. Phys. **40**, 123 (2014).
[39] T. Akazawa, T. Suzuki, H. Goshima, T. Tahara, T. Fujita, T. Takabatake, and H. Fujii, J. Phys. Soc. Jpn. **67**, 3256 (1998).
[40] T. Suzuki, I. Ishii, N. Okuda, K. Katoh, T. Takabatake, T. Fujita, and A. Tamaki, Phys. Rev. B **62**, 49 (2000).
[41] B. Lüthi, in *Dynamical Properties of Solids*, edited by G. K. Horton and A. A. Maradudin (North-Holland, Amsterdam, 1980), Vol. 3.
[42] N. V. Hieu, T. Takeuchi, H Shishido, C. Tonohiro, T. Yamada, H. Nakashima, K. Sugiyama, R. Settai, T. D. Matsuda, Y. Haga, M. Hagiwara, K. Kindo, S. Araki, Y. Nozue, and Y. Onuki, J. Phys. Soc. Jpn. **76**, 064702 (2007).
[43] M. T. Hutchings, Solid State Phys. **16**, 227 (1964).
[44] M. Nohara, T. Suzuki, Y. Maeno, T. Fujita, I. Tanaka, and H. Kojima, Phys. Rev. B **52**, 570 (1995).
[45] See Supplemental Material at http://link.aps.org/supplemental/10.1103/PhysRevB.99.054413 for information about the crystal-electric-field analysis.
[46] J. J. M. Franse, Helv. Phys. Acta **56**, 131 (1983).
[47] J. Lee, M. Matsuda, J. A. Mydosh, I. Zaliznyak, A. I. Kolesnikov, S. Süllow, J. P. C. Ruff, and G. E. Granroth, Phys. Rev. Lett. **121**, 057201 (2018).
[48] H. Hill, in *Plutonium*, edited by W. N. Miner (AIME, New York, 1970), p. 2.
[49] L. Havela, J. Hřebík, J. Šternberk, A. Meňovský, and A. Zentko, Phys. Status Solidi A **59**, K165 (1980).
[50] H. Nakotte, A. Purwanto, R. A. Robinson, Z. Tun, K. Prokeš, A. C. Larson, L. Havela, V. Sechovský, H. Maletta, E. Brück, and F. R. de Boer, Phys. Rev. B **54**, 7201 (1996).
[51] M. S. Henriques, D. I. Gorbunov, J. C. Waerenborgh, L. Havela, A. B. Shick, M. Diviš, A. V. Andreev, and A. P. Gonçalves, J. Phys.: Condens. Matter **25**, 066010 (2013).
[52] M. S. Henriques, D. I. Gorbunov, A. V. Andreev, Z. Arnold, S. Surblé, S. Heathman, J. C. Griveau, E. B. Lopes, J. Prchal, L. Havela, and A. P. Gonçalves, Phys. Rev. B **89**, 054407 (2014).
[53] B. R. Cooper, R. Siemann, D. Yang, P. Thayamballi, and A. Banerjea, in *Handbook on the Physics and Chemistry of the Actinides*, edited by A. J. Freeman and G. H. Lander (Elsevier, Amsterdam, 1985), Vol. 2.
[54] S. C. Miller and W. F. Love, *Tables of Irreducible Representations of Space Groups and Co-Representations of Magnetic Space Groups* (Pruett, Boulder, 1967); see also A. P. Cracknell, B. L. Davies, S. C. Miller, and W. F. Love, *Kronecker Product Tables*w (Plenum, New York, 1979), Vol. 1.
[55] J. M. Perez-Mato, S. V. Gallego, E. S. Tasci, L. Elcoro, G. de la Flor, and M. I. Aroyo, Annu. Rev. Mater. Res. **45**, 217 (2015).
[56] S. V. Galego, J. M. Perez-Mato, L. Elcoro, E. S. Tasci, R. M. Hansen, K. Momma, M. I. Aroyo, and G. Madariaga, J. Appl. Crystallogr. **49**, 1750 (2016).
[57] R. A. Robinson, A. C. Lawson, J. W. Lynn, and K. H. J. Buschow, Phys. Rev. B **47**, 6138 (1993).
[58] L. M. Sandratskii and G. H. Lander, Phys. Rev. B **63**, 134436 (2001).
[59] V. Sechovský, L. Havela, A. Purwanto, A. C. Larson, R. A. Robinson, K. Prokeš, H. Nakotte, E. Brück, F. R. de Boer, P. Svoboda, H. Maletta, and M. Winkelmann, J. Alloys Compd. **213-214**, 536 (1994).
[60] G. M. Kalvius, D. R. Noakes, S. El-Khatib, E. J. Ansaldod, C. E. Stronach, E. Brück, and H. Nakotte, J. Alloys Compd. **441**, 11 (2007).
[61] A. Purwanto, V. Sechovský, L. Havela, R. A. Robinson, H. Nakotte, A. C. Larson, K. Prokeš, E. Brück, and F. R. de Boer, Phys. Rev. B **53**, 758 (1996).